Room temperature tetragonal noncollinear antiferromagnet Pt_2MnGa

S. Singh,[1] S. W. D'Souza,[1] E. Suard,[2] L. Chapon,[2] A. Senyshyn,[3]
V. Petricek,[4] Y. Skourski,[5] M. Nicklas,[1] C. Felser,[1] and S. Chadov[1]

[1]*Max Planck Institute for Chemical Physics of Solids, Nöthnitzer Str. 40, D-01187 Dresden, Germany*
[2]*Institut Laue-Langevin, BP 156, 38042 Grenoble Cedex 9, France*
[3]*Forschungsneutronenquelle Heinz Maier-Leibnitz FRM-II,*
Technische Universität München, Lichtenbergstrasse 1, 85747 Garching, Germany
[4]*Institute of Physics ASCR, Department of Structure Analysis, Na Slovance 2, 18221 Praha, Czech Republic*
[5]*Dresden High Magnetic Field Laboratory (HLD-EMFL),*
Helmholtz-Zentrum Dresden-Rossendorf, D-01328 Dresden, Germany

Here we present the tetragonal stoichiometric Heusler compound Pt_2MnGa with the noncollinear AFM order stable up to 350 K. It is resolved by the neutron diffraction as a helical spiral propagating along the tetragonal axis. *Ab-initio* calculations suggest a pure exchange origin of the spiral and explain its helical character being stabilized by a large basal plane magnetocrystalline anisotropy (MCA). Together with the inversion-symmetric crystal structure, this provides a bi-stability of a spiral with respect to the right- and left-handed magnetic helices. Despite the large MCA, the long period of a helix might greatly facilitate the switch of the helicity by the precessional reorientation, suggesting Pt_2MnGa as a potential candidate for the vector-helicity based non-volatile magnetic memory.

Antiferromagnets (AFMs) gain an increasing attention in the state-of-the-art applied and academic research. Their auxiliary role of a static support, enhancing the hardness of ferromagnetic electrodes through the exchange bias effect in the conventional microelectronics, has been broadly extended by the new prospectives in spintronics applications. For instance, by studying the magnetoresistance effects typically exploited in spintronics [1], it has been demonstrated that Ir-Mn AFM, utilized as an active medium in a tunneling magnetoresistance device, exhibits a 160 % tunneling anisotropic magnetoresistance at 4 K in weak magnetic fields of 50 mT or less. AFMs also facilitate the current-induced switching of their order parameter [2–4] due to the absence of the shape anisotropy and the action of spin torques through the entire volume. For instance, a relatively low critical current density of $4.6\,\mathrm{MA/cm^2}$ was reported for the collinear AFM CuMnAs [5]. Additional nontrivial spintronic effects originating from a non-vanishing Berry phase might occur in the noncollinear AFMs [6]. For instance, the noncollinear planar AFMs with the absence of mirror symmetry, such as Mn_3Ir, where predicted to exhibit the anomalous Hall [7, 8], Kerr and other effects characterized by the same spatial tensor shape [9], which where not encountered in AFM systems so far.

Another set of specific properties, alternative to the above mentioned systems, are provided by one-dimensional long-range AFM modulations, such as cycloidal - $\vec{q} \perp (\vec{e}_i \times \vec{e}_j)$ and screw (or helical) - $\vec{q} \parallel (\vec{e}_i \times \vec{e}_j)$, with $\vec{e}_{i,j}$ being the spin directions on i and j neighboring atomic sites sitting along the spiral propagation vector $\vec{q}$. These systems possess a specific order parameter $\vec{\kappa}_{ij} = \vec{e}_i \times \vec{e}_j$, denoted as "chirality" or "helicity". E.g., in cycloidal AFM insulators $\vec{\kappa}$ is coupled to the polarization vector $\vec{P} \sim \vec{q} \times \vec{\kappa}$, by leading to the first-order ferroelectic effect [10–13]. For the screw-spiral order ($\vec{q} \times \vec{\kappa} = 0$) it becomes possible only upon the additional specific condition, namely, when the crystal structure remains invariant under inversion and rotations around $\vec{\kappa}$, but non-invariant under 180° rotation of the $\vec{\kappa}$-axis [14, 15]. The information transfer in cycloidal spirals along the one-dimensional atomic chains with the fixed $\vec{\kappa}$, stabilized by the surface Dzyaloshinskii-Moriya mechanism, was demonstrated by switching their phase with external magnetic field [16]. Such scheme is inapplicable to the screw spirals due to their energy degeneracy with respect to the $\vec{\kappa}$ reversal, even if they are deposited on a surface [17]. Similar to the situation with the ferroelectric effect, to fix a helicity of the screw spiral would require additional symmetry constrains on the crystal structure [18]. Despite that the cycloidal order seems to be more ubiquitous for the applications, the aforementioned degeneracy between the left- and right-handed magnetic screws in crystals with inversion symmetry might be considered as an alternative advantage. In particular, it allows to directly associate a bit of information with the helicity. The switch of $\vec{\kappa}$ can be realized e.g., by an external magnetic pulse $\vec{H}_{\mathrm{ext}} \perp \vec{\kappa}$ which reorients the spins precessionally (see Fig. 1). In this case, both stable $\pm\vec{\kappa}$ states would be connected over the energy barrier representing the cycloidal-ordered state.

Here we report on a similar AFM spiral magnetic order in the tetragonal Pt_2MnGa Heusler system, revealed by the neutron diffraction. The present first-principles analysis justifies the non-relativistic exchange origin of a spiral, confirms its experimentally deduced wave-vector $\vec{q} \approx (0, 0, 1/5)$ in units of $2\pi/c$ and suggests the screw-type order caused by a moderate hard axis (tetragonal c-axis) magnetocrystalline anisotropy (MCA).

To our knowledge, there are no reliable experimental

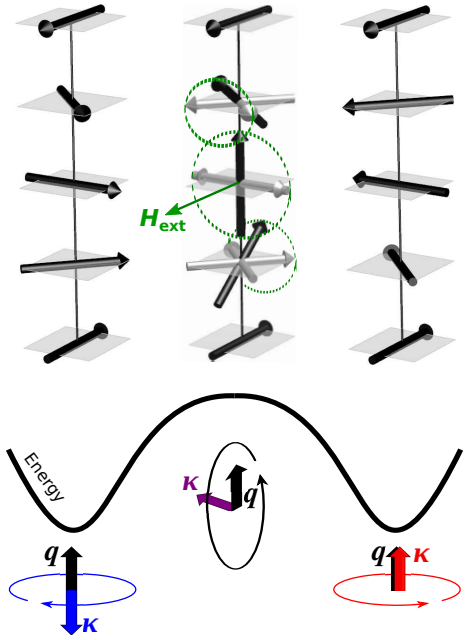

FIG. 1: Application of the external magnetic pulse $\vec{H}_{\rm ext}$ perpendicular to the spiral wave vector $\vec{q}$ causes the precession of local moments (along the dashed green circles). In case of the easy-plane MCA, the long period of a spiral greatly facilitates reorientation of helicity from $\vec{\kappa} \uparrow\downarrow \vec{q}$ (blue) to $\vec{\kappa} \uparrow\uparrow \vec{q}$ (red) or vice versa, since the top of the energy barrier between two stable screws is a cycloid $\vec{\kappa} \perp \vec{q}$ (magenta), in which only few atomic planes with magnetic moments orthogonal to $\vec{H}_{\rm ext}$ acquire the high energy.

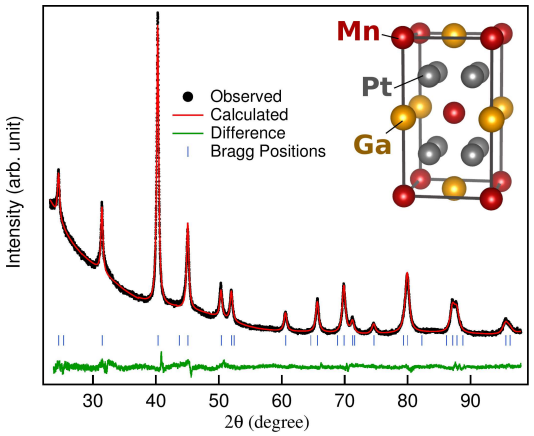

FIG. 2: Crystal structure of Pt_2MnGa. Rietveld refinement of the room-temperature XRD pattern assuming the tetragonal unit cell with $I4/mmm$ symmetry. Observed and calculated patterns, as well as their difference are shown by black open circles, red and green solid lines, respectively. Blue vertical ticks indicate the Bragg peak positions. The sketch of the unit cell is shown in the inset: red, yellow and gray spheres indicate Mn, Ga and Pt atoms in 2*a*, 2*b* and 4*d* Wyckoff positions, respectively.

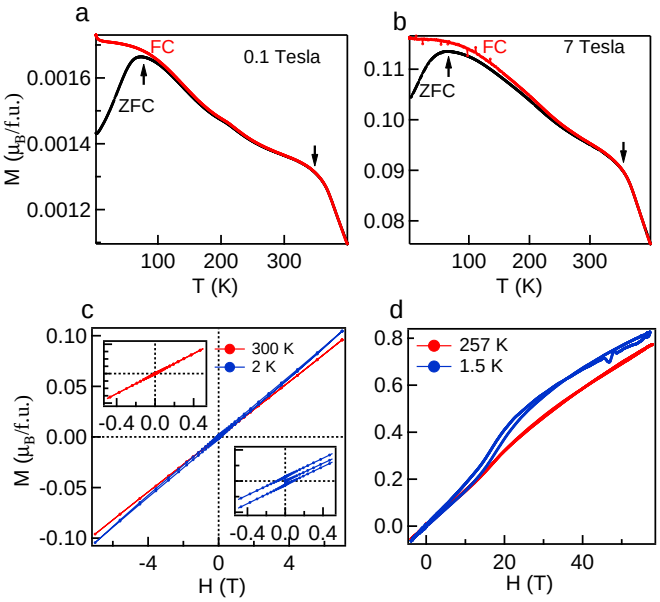

FIG. 3: Magnetization of Pt_2MnGa as a function of temperature T and magnetic field H: $M(T)$ at (a) 0.01 T and (b) 7 T; (c) at 300 K and 2 K up to 7 T; $M(H)$ in the magnetic pulse of 60 T at 257 K and 1.5 K (d).

results on this material in the literature. The single old report on Pt_2MnGa [19] briefly refers it as $L2_1$ AFM with $T_N = 75$ K, but no further details are given. Later on, Pt_2MnGa has been studied by *ab-initio* assuming ferromagnetic ordering and revealed that the tetragonal phase is more stable [20, 21]. In [20] it was only mentioned that in $Pt_xNi_{2-x}MnGa$ alloy series "the AFM correlations become stronger by increasing x". In more recent *ab-initio* study [22] the nearest neighbor AFM order was found to be noticeably higher in energy compared to the ferromagnetic. To clear the actual crystal and magnetic structure we prepared a polycrystalline Pt_2MnGa sample (details are given in the Supplementary). The room-temperature crystal structure (Fig. 2) was deduced from the Rietveld refinement of the x-ray diffraction data. All Bragg reflections can be indexed by assuming the tetragonal space group $I4/mmm$. The refined lattice parameters are $a = b = 4.02$ Å, $c = 7.24$ Å; Pt occupies $4d$ $(0, 1/2, 1/4)$, while Mn and Ga - $2a$ $(0, 0, 0)$ and $2b$ $(0, 0, 1/2)$ Wyckoff sites, respectively (see the inset in Fig. 2).

The low-field $M(T)$ curves measured within the zero-field-cooled (ZFC) and field-cooled (FC) cycles are shown in Fig. 3 a. The ZFC $M(T)$ shows a maximum at $T \approx 65$ K, absent in the FC regime. This observation typical for many Heusler alloys results from the polycrystalline configuration of the anisotropic crystallites. The high-temperature behavior is similar in both ZFC and FC regimes and indicates the change of the magnetic ordering at 350 K. Overall, the amplitude of $M(T)$ is very small in both ZFC and FC regimes, even at low temperatures (2 K) and higher fields (7 T), (Fig. 3 b). Both isothermal $M(H)$ curves at 300 K (Fig. 3 c) and 2 K

(Fig. 3 d) exhibit a non-saturating (straight line) increase up to 7 T, similar to the antiferromagnetic or paramagnetic materials. Only a narrow field hysteresis (Fig. 3 d, inset) indicates a very weak ferromagnetism at low temperature (2 K). To probe the behavior of the system at very high magnetic fields, we performed the 60 T pulse measurements. Corresponding $M(H)$ curves measured at 257 and 1.5 K (Fig. 3 e, f) also do not exhibit any saturation, by scaling almost linearly with the field. Only at 1.5 K a small hysteresis within $0 < H < 35$ T is observed indicating the metamagnetic transition around 14 T induced by the non-equilibrium magnetic pulse. All this clearly suggests that Pt_2MnGa is not a ferromagnet.

To determine the actual magnetic order, the powder neutron diffraction measurements were performed at 500 K (above the magnetic ordering), 300 K and 3 K. The crystal structure refinement of Pt_2MnGa of powder neutron diffraction data at 500 K gives similar results as of the room-temperature XRD, however, the substantial difference in the nuclear scattering amplitude (of 0.96, −3.73, and 7.29 fm for Pt, Mn, and Ga, respectively) suggests a certain degree of disorder to be present in the actual atomic occupancies. Fig. 4 a shows a comparison of the Rietveld refinement with the high-temperature spectrum for (002) and (110) Bragg peaks, assuming several different configurations. The chemically ordered model gives a clear mismatch in the fit (upper panel of Fig. 4 a), the presence of random Mn(2*a*)-Pt(4*d*) disorder does not improve it either. The most reasonable agreement gives a model with 33 % of Mn(2*a*)-Ga(2*b*) disorder (lower panel in Fig. 4 a). The refinement details for the full range diffraction pattern at 500 K is given in the Supplementary.

By going to lower temperatures, we assumed the magnetic unit cell with two Mn types in 2*a* and 2*b* sites having corresponding occupancies. The Rietveld refinement of the magnetic phases observed at 300 and 3 K was performed by accounting for the magnetic and atomic structures simultaneously. The comparison within a narrow angular range $20° < 2\theta < 35°$ between 500, 300 and 3 K neutron diffraction patterns is given in Fig. 4 b. At 300 and 3 K, the long-range magnetic ordering is evidenced by the presence of two additional Bragg peaks, at $2\theta \approx 24.1°$ and 29.3° (indicated by the red arrows at 300 and 2 K in Fig. 4 b), which closely corresponds to the commensurate reciprocal vector $\vec{q} = (0,\ 0,\ 1/5)$ in units of $2\pi/c$. Precise analysis reveals slightly incommensurate temperature-dependent variation: $\vec{q} = (0,\ 0,\ 0.2066(1))$ at 300 K and $(0,\ 0,\ 0.19(5))$ at 3 K.

To specify more details of the magnetic ground state, we focus on the 3 K data exhibiting the highest intensity of the magnetic Bragg peaks. Its analysis suggests that the spiral order of the magnetic moments on Mn atoms (in 2*a* and 2*b*) would be more favorable, as it delivers the magnetic moments amplitudes close to a reasonable Mn value of $4\,\mu_B$. In contrast, the collinear spin-wave model leads to the values substantially exceeding $5\,\mu_B$. In the next step, we tried to distinguish which type of a spin spiral is more preferable. By assuming the spiral magnetic structure rotating in the *bc*-plane (cycloidal spiral) we obtained the moments of $4.33(13)\,\mu_B$ for both Mn in 2*a* and 2*b* sites. Although these values are acceptable, they slightly exceed those reported in the literature for Mn(2*a*) in Mn-based Heusler alloys. Finally, by assuming the spiral rotating within the *ab*-plane (screw spiral) leads to $3.93(11)\,\mu_B$, a value which is somehow closer to those reported in the literature. Since the rigorous experimental answer requires the polarized neutron spectroscopy data, in the following we will focus on the first-principle analysis.

To complete the experimental information we computed the $\vec{q}$-dependent total energies using the *ab-initio* LMTO method [23] adopting the local spin-density approximation to the exchange-correlation [24]. Since the method assumes perfectly ordered systems, we do not account for Mn/Ga chemical disorder indicated by neutron scattering. The unit cell parameters were taken from the present experimental refinement.

First, we determined the preferential $\vec{q}$ vector. Since the parameters of the present magnetic modulation are defined mostly by the interplay of the isotropic exchange interactions which have a largest energy scale (note, that the anisotropic Dzyaloshinskii-Moriya interactions must be largely canceled by crystal symmetry), it is practical to perform the non-relativistic calculations first. The absence of the spin-orbit coupling allows to apply the generalized Bloch theorem and to study the spin spirals within the chemical unit cell without going to the large supercells. The energy dispersion computed along several symmetric directions is shown in Fig. 5 a. In order to plot several curves along the same coordinate axis, we give the q length in the $2\pi/d$ units, where d is the distance between the nearest Mn-containing atomic planes orthogonal to $\vec{q}$. In this notation, $q = 0.5$ always corresponds to the antiparallel orientation of the spin moments in the nearest planes. As we see from Fig. 5 a, the energy dispersion in the *ab*-plane ([100] and [110] directions) is monotonous, being characterized by a single minimum at $q = 0$ (ferromagnet) and a single maximum at $q = 0.5$ (shortest AFM order). For the out-of-*ab*-plane directions one observes a formation of a local minimum within $0 < q < 0.5$. Whereas along [111] direction it forms at rather high energy, along [001] (*c*-axis) it turns to global, supporting the experimental conclusions. Energy minimum vector is $\vec{q} \approx (0, 0, 0.11) = (0, 0, 0.22 \cdot (2\pi/c))$ (see also a more detailed plot in Fig. 5 b), which is very close to the experimental one $\vec{q} \approx (0, 0, 1/5 \cdot (2\pi/c))$. Additional Monte-Carlo simulation of the classical Heisenberg model parametrized by the *ab-initio* exchange coupling constants (see the Supplementary) reasonably reproduces the magnetic ordering temperature ($T_N \approx 350$ K) and reveal that the AFM order is set by the interplay be-

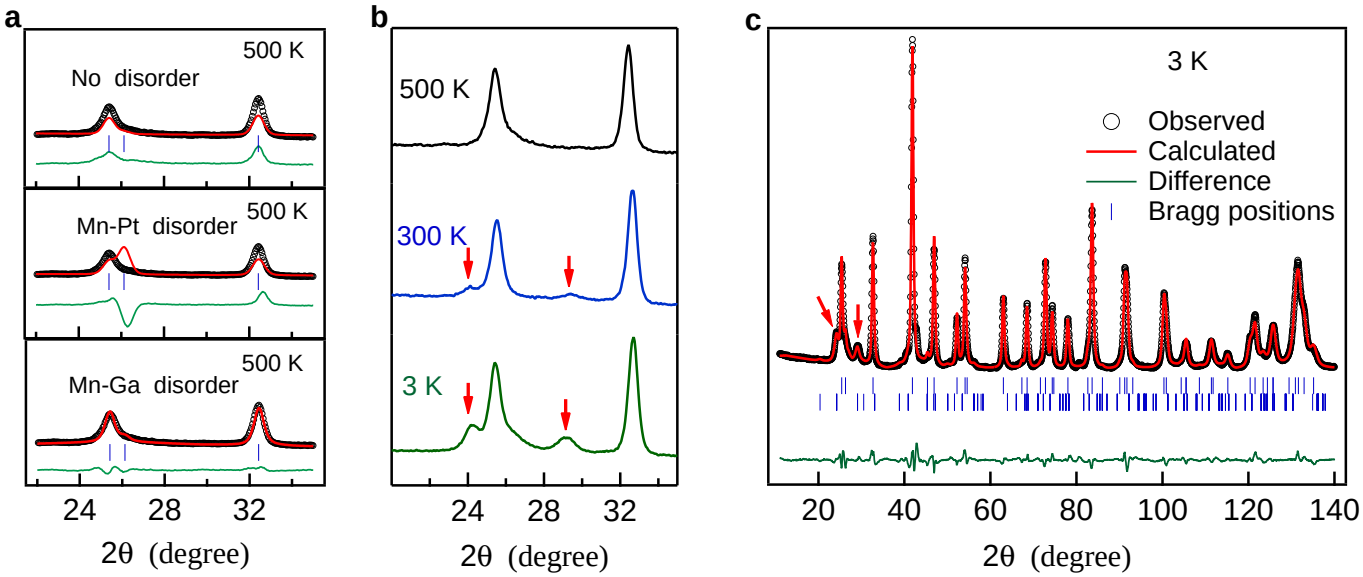

FIG. 4: Powder neutron diffraction studies on Pt_2MnGa. (a) Rietveld refinements of 500 K neutron diffraction pattern where the (002) and (110) Bragg peaks (black circles) have been fitted (red solid lines) by assuming (i) no disorder, (ii) Mn($2a$)/Pt($4d$) disorder, and (iii) Mn($2a$)/Ga($2b$) disorder. The green curve shows the difference between observed and calculated patterns. Vertical ticks are nuclear Bragg peak positions. (b) Comparison of neutron diffraction patterns at 500, 300 and 2 K. Magnetic peaks are indicated by red arrows at 300 and 2 K. (c) The observed (black circle) and modeled (red solid line) neutron diffraction pattern for Pt_2MnGa at 3 K. The vertical arrows indicate the magnetic peaks. Upper vertical ticks are nuclear Bragg peak positions; lower vertical - magnetic.

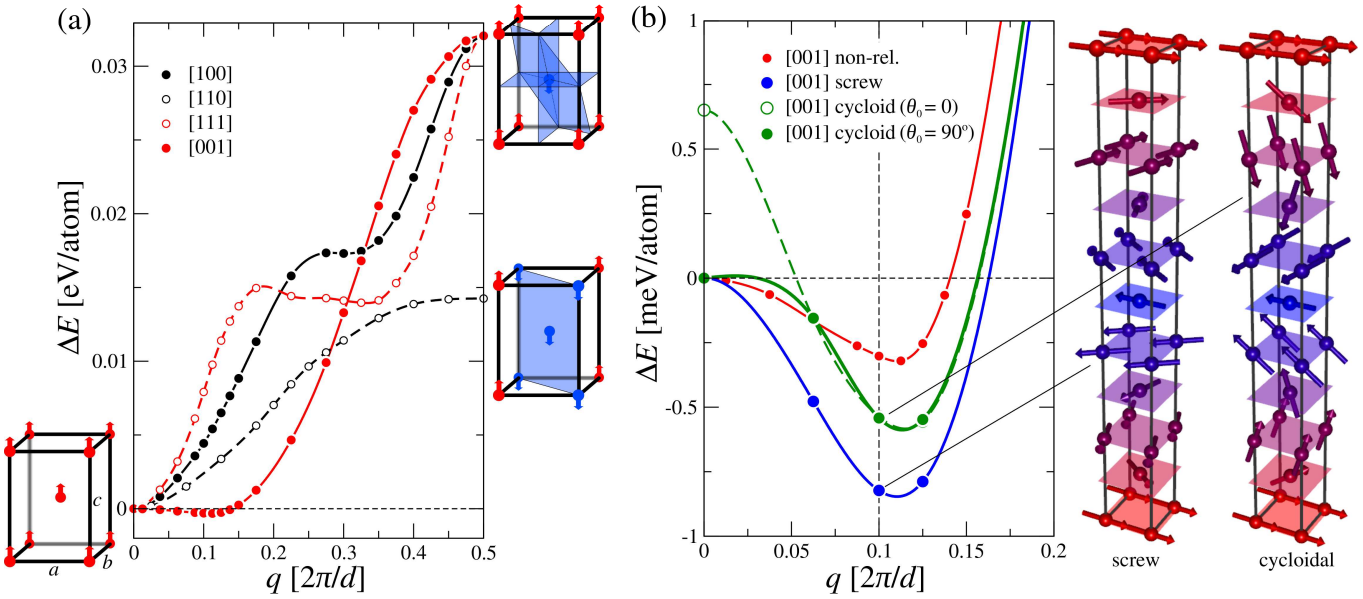

FIG. 5: Total energies ΔE calculated as functions of $\vec{q}$ (in units of $2\pi/d$, where d is the distance between the nearest Mn-containing planes orthogonal to $\vec{q}$). (a) Non-relativistic regime: black solid and dashed lines refer to [100] ($d = a/2$) and [110] ($d = a/\sqrt{2}$) directions; red dashed and solid lines - to [111] ($d = (c/2)/\sqrt{2(c/a)^2 + 1}$) and [001] ($d = c/2$) directions, respectively. The energy zero is taken at $q = 0$ (ferromagnet). (b) Detailed comparison of different regimes along [001]: red, blue and green lines/points refer to the non-relativistic (same as [001] in (a)), screw- and cycloidal-type spirals, respectively. Cycloidal order has two variants: the first one (dashed green line, open circles) which represents at $q = 0$ a hard-c-axis oriented ferromagnetic state ($\theta_0 = 0$); the second one (solid green line, filled circles) represents at $q = 0$ an easy-ab-plane oriented ferromagnetic state ($\theta_0 = 90°$). The energy zero corresponds to the easy-ab-plane ferromagnetic order. All lines are given for an eye guide. For several specific configurations the Mn($2a$) magnetic sublattice is shown explicitly; spin moments are colored from red to blue according to their phase.

tween the strong short-range parallel and the weaker long-range (7-th shell) antiparallel interactions along the c-axis within the $2a$ sublattice.

Next, we determine the type of the spin spiral (screw- or cycloidal), which results from the relativistic effects. In this case the Bloch theorem does not hold and the magnetic order can be studied only in supercells. Since in this case we can account only for the commensurate modulations, the supercells must be sufficiently large to provide the energies at long wavelengths: a minimal supercell hosting a $(0, 0, 1/5 \cdot (2\pi/c))$ modulation contains at least five standard units. As we see from Fig. 5 b, the relativistic effects substantially deepen the spiral energy minimum and almost do not change the corresponding $\vec{q}$ vector ($q \approx 0.11$). The ab-plane appears to be an easy plane, since the screw-type spiral is more preferable in the whole range of the wavelengths. The energy difference between the cycloidal and the screw spirals is contributed by the MCA energy which has a rather large magnitude for the Heusler class, being close to 0.65 meV/atom (or 2.6 meV/f.u.) at $q = 0$. At the global minimum this energy difference is reduced more than twice. Due to the hard-c-axis MCA, the cycloidal spiral can still be optimized in terms of a homogeneity (which must be distorted by the MCA), however it will have a higher energy compared to the screw order anyway. At the same time, as it is follows from the growing energy difference between $\theta_0 = 0$ and 90° cases, the phase optimization of the cycloidal spiral makes sense only for the small $q < 0.06$, far from the global minimum. The amplitude of the Mn magnetic moment in the screw spiral has a tendency to grow by going from $q = 0$ (ferromagnetic) towards $q = 0.5$ (shortest AFM order), though its absolute increase is relatively small: from about 3.7 to 3.8 μ_B, which agrees with neutron data refinement.

To conclude, we present a newly synthesized stoichiometric tetragonal ($I4/mmm$) Pt_2MnGa Heusler system exhibiting the room-temperature AFM spiral order with the wave vector $\vec{q} = (0, 0, 1/5 \cdot 2\pi/c)$, as it follows from the neutron-diffraction refinement analysis. Certain degree ($\sim 30\,\%$) of Mn-Ga chemical disorder was indicated. *Ab-initio* calculations (assuming the ordered system) reasonably reproduce the experimental $\vec{q}$ vector indicating the exchange origin of the spiral. Monte-Carlo simulations of the classical Heisenberg model parametrized with the *ab-initio* exchange coupling constants reasonably reproduce the Neel temperature and suggest the long-range antiparallel Mn-Mn exchange (beyond the 6-th Mn shell) as a driving mechanism for the AFM order. Relativistic calculations indicate an easy-ab-plane MCA, which stabilizes the screw (proper screw, or fully helical) spiral type. Due to inversion symmetry, the left- and right-handed spirals are stable and degenerate in energy. In spite of a large MCA, the energy barrier between them can be efficiently overcome via the precessional magnetization reorientation induced by the magnetic pulse perpendicular to the spiral axis. In this case, the barrier reduces to the energy difference between the screw and cycloidal spiral orders. In particular, this suggests Pt_2MnGa as a convenient candidate for the non-volatile magnetic memory based on the helicity vector as a bit of information.

S.S. thanks to Alexander von Humboldt foundation for fellowship. S.C. thanks to A.N. Yaresko (MPI-FKF Stuttgart) for providing his program code and discussions. The work was financially supported by the ERC AG 291472 "IDEA Heusler!"

[1] B. G. Park, J. Wunderlich, X. Martí, V. Holý, Y. Kurosaki, M. Yamada, H. Yamamoto, A. Nishide, J. Hayakawa, H. Takahashi, et al., Nature Mat. **10**, 347 (2011).
[2] A. S. Núñez, R. A. Duine, P. Haney, and A. H. MacDonald, Phys. Rev. B **73**, 214426 (2006).
[3] H. V. Gomonay and V. M. Loktev, Phys. Rev. B **81**, 144427 (2010).
[4] E. V. Gomonay and V. M. Loktev, J. Low Temp. Phys. **40**, 17 (2014).
[5] P. Wadley, B. Howells, J. Železný, C. Andrews, V. Hills, R. P. Campion, V. Novák, K. Olejník, F. Maccherozzi, S. S. Dhesi, et al., Science (2016).
[6] O. Gomonay, Phys. Rev. B **91**, 144421 (2015).
[7] H. Chen, Q. Niu, and A. H. MacDonald, Phys. Rev. Lett. **112**, 017205 (2014).
[8] J. Kübler and C. Felser, Europhys. Lett. **108**, 67001 (2014).
[9] M. Seemann, D. Ködderitzsch, S. Wimmer, and H. Ebert, Phys. Rev. B **92**, 155138 (2015).
[10] H. Katsura, N. Nagaosa, and A. V. Balatsky, Phys. Rev. Lett. **95**, 057205 (2005).
[11] M. Kenzelmann, A. B. Harris, S. Jonas, C. Broholm, J. Schefer, S. B. Kim, C. L. Zhang, S.-W. Cheong, O. P. Vajk, and J. W. Lynn, Phys. Rev. Lett. **95**, 087206 (2005).
[12] M. Mostovoy, Phys. Rev. Lett. **96**, 067601 (2006).
[13] I. A. Sergienko and E. Dagotto, Phys. Rev. B **73**, 094434 (2006).
[14] T. Arima, J. Phys. Soc. Japan **76**, 073702 (2007).
[15] R. D. Johnson, L. C. Chapon, D. D. Khalyavin, P. Manuel, P. G. Radaelli, and C. Martin, Phys. Rev. Lett. **108**, 067201 (2012).
[16] M. Menzel, Y. Mokrousov, R. Wieser, J. E. Bickel, E. Vedmedenko, S. Blügel, S. Heinze, K. von Bergmann, A. Kubetzka, and R. Wiesendanger, Phys. Rev. Lett. **108**, 197204 (2012).
[17] K. von Bergmann, A. Kubetzka, O. Pietzsch, and R. Wiesendanger, J. Phys.: Condens. Matter **26**, 394002 (2014).
[18] S. V. Grigoriev, N. M. Potapova, S.-A. Siegfried, V. A. Dyadkin, E. V. Moskvin, V. Dmitriev, D. Menzel, C. D. Dewhurst, D. Chernyshov, R. A. Sadykov, et al., Phys. Rev. Lett. **110**, 207201 (2013).
[19] F. A. Hames and J. Crangle, J. Appl. Physics **42**, 1336 (1971).
[20] M. Siewert, M. E. Gruner, A. Dannenberg, A. Chakrabarti, H. C. Herper, M. Wuttig, S. R.

Barman, S. Singh, A. Al-Zubi, T. Hickel, et al., Appl. Phys. Lett. **99**, 191904 (2011).
[21] L. Feng, E. K. Liu, W. X. Zhang, W. H. Wang, and G. H. Wu, J. Magn. Magn. Materials **377**, 40 (2015).
[22] T. Roy and A. Chakrabarti, J. Magn. Magn. Materials **401**, 929 (2016).
[23] A. Perlov, A. Yaresko, and V. Antonov, *Spin-polarized Relativistic Linear Muffin-tin Orbitals Package for Electronic Structure Calculations, PY-LMTO.* (unpublished).
[24] S. H. Vosko, L. Wilk, and M. Nusair, Can. J. Phys. **58**, 1200 (1980).

Supplementary information
Room temperature tetragonal noncollinear antiferromagnet Pt_2MnGa

S. Singh,[1] S. W. D'Souza,[1] E. Suard,[2] L. Chapon,[2] A. Senyshyn,[3]
V. Petricek,[4] Y. Skourski,[5] M. Nicklas,[1] C. Felser,[1] and S. Chadov[1]

[1]*Max Planck Institute for Chemical Physics of Solids, Nöthnitzer Str. 40, D-01187 Dresden, Germany*
[2]*Institut Laue-Langevin, BP 156, 38042 Grenoble Cedex 9, France*
[3]*Forschungsneutronenquelle Heinz Maier-Leibnitz FRM-II,*
Technische Universität München, Lichtenbergstrasse 1, 85747 Garching, Germany
[4]*Institute of Physics ASCR, Department of Structure Analysis, Na Slovance 2, 18221 Praha, Czech Republic*
[5]*Dresden High Magnetic Field Laboratory (HLD-EMFL),*
Helmholtz-Zentrum Dresden-Rossendorf, D-01328 Dresden, Germany

EXPERIMENTAL DETAILS

Polycrystalline ingot of Pt_2MnGa was prepared by melting appropriate quantities of Pt, Mn and Ga of 99.99% purity in an arc furnace. Ingots were then annealed at 1273 K for 5 days to obtain homogeneity and subsequently quenched into ice water. Powder x-ray diffraction (XRD) at room temperature (RT)was done to investigate the sample quality and homogeneity using CuKα radiation. The composition of the sample was confirmed using energy dispersive analysis of x-rays (EDAX) analysis which gave a composition $Pt_{50.98}Mn_{25.05}Ga_{23.98}$ ($Pt_{2.04}Mn_{1.0}Ga_{0.96}$), which we refer to as Pt_2MnGa henceforth in the manuscript. The temeprature dependent ($M(T)$) and field dependent ($M(H)$) magnetization measurements were done using SQUID-VSM magnetometer. The low-field $M(T)$ curves measured within the zero-field-cooled (ZFC) and field-cooled (FC) cycles For the ZFC-measurement, the sample was cooled in zero field down to 2 K and after 0.1 T field was applied and then the data were recorded in heating cycle up to 400 K. Subsequently, the data were recorded in the same field (0.1 T) by cooling from 400 down to 2 K (FC).The magnetic isotherms, M(H), at 1.2 K and 257 K have been done in a pulsed fields up to 60 T. The pulsed magnetic field experiments were performed at the Dresden High Magnetic Field Laboratory. Neutron diffraction measurements were done at the D2B high-resolution neutron powder diffractometer (ILL, Grenoble). A vanadium cylinder was used as sample holder. The data were collected at 500 K, 300 K and 3 K using a neutron wavelength of 1.59 Å in the high-intensity mode. The analysis of diffraction patterns were done with Fullprof software package[1].

Nuclear structure from neutron diffraction

Fig. 1 shows the observed and calculated neutron diffraction pattern of at 500 K (paramagnetic phase) in the 2θ range of 20-100°. All the neutron diffraction peaks can be indexed well by the tetragonal unit cell with refined lattice parameters are $a = b = 4.03$ Å, $c = 7.23$ Å. The Rietveld refinement was performed using space group $I4/mmm$ as in case of x-ray diffraction. In order case the Pt occupy the $4d$ $(0, 0.5, 0.25)$ position, while Mn and Ga occupied at $2a$ $(0, 0, 0)$ and $2b$ $(0, 0, 0.5)$ Wyckoff positions, respectively. However, the Rietveld analsyis shows that a substantial (33%) Mn($2a$)-Ga($2b$) antisite disorder exist in the sample. Therefore,33% Mn occupied at Ga ($2b$) site and similarly 30% Ga occupied at Mn $2a$ site.

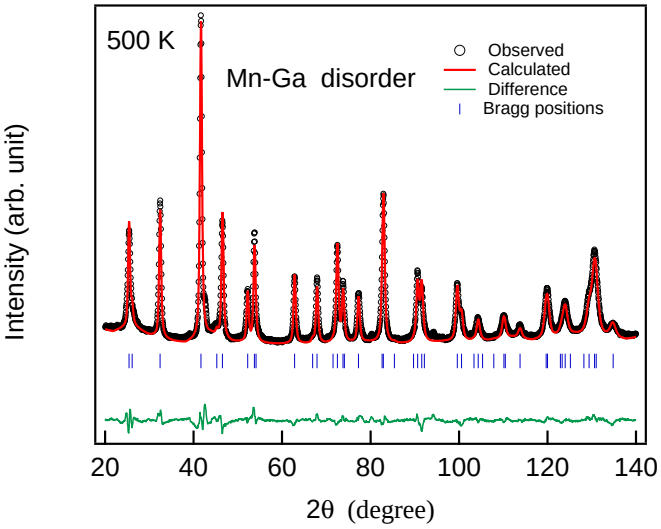

FIG. 1: Rietveld refinement of powder neutron diffraction pattern of 500 K in the 2θ range of 20-100°. The observed, calculated and difference patterns are shown by black,red and green solid lines, respectively. The vertical ticks indicate the nuclear Bragg peak positions.

THEORETICAL DETAILS

It is instructive to understand which mechanisms are responsible for setting such ground-state modulation. Since the relativistic effects do not affect the ground-state $\vec{q}$ vector substantially, in the following we will calculate the isotropic exchange coupling constants J using the

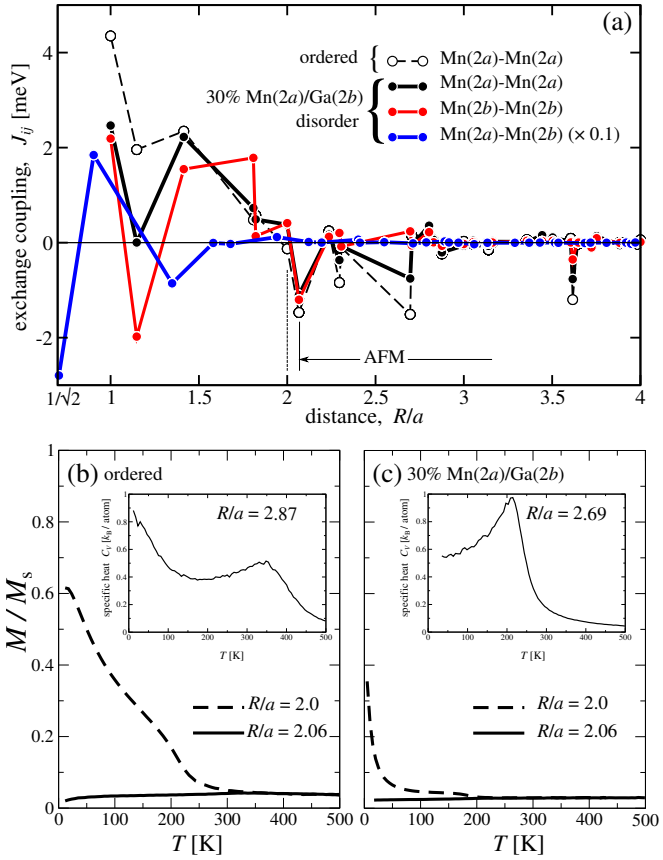

FIG. 2: (a) Isotropic exchange coupling constants J_{ij} calculated as functions of distance R (in the units of a) between i and j Mn sites for the fully ordered and partially disordered cases. (b) and (c) represent the Monte-Carlo simulated M/M_S temperature dependencies of the Heisenberg model parametrized by the computed J_{ij}, in the fully ordered and partially disordered cases, respectively. Solid line corresponds to the minimal cluster size needed to set the AFM order, dashed - by one shall smaller cluster. The insets show the temperature dependency of the specific heat C_V (computed for the largest cluster size) which indicates the position of T_N by the local maximum.

real-space approach [2] implemented in the SPR-KKR Green's function method [3]. In Fig. 2 a they are plotted as functions of distance between the interacting sites i and j. Here, we drop all interactions involving Pt and Ga atoms as insignificant, by leaving only those between Mn atoms. In the fully ordered case, all nearest Mn(2a)-Mn(2a) interactions are parallel ($J > 0$), whereas the antiparallel ones ($J < 0$) are encountered by starting from $R/a = 2$ (6-th shell within (2a)-sublattice). As it is shown by $M(T)/M_S$ curves (Fig. 2 b) obtained by the Monte-Carlo simulation (ALPS package [4]) of the classical Heisenberg model ($H = -\sum_{i>j} J_{ij}\, \vec{e}_i \cdot \vec{e}_j$, where $\vec{e}_{i,j}$ are the unity vectors along the local magnetization directions on i and j sites), the AFM order sets in by including all interactions at least up to $R/a \approx 2.06$ (7-th shell); accounting of the higher shells does not affect the $M(T)$ behavior anymore. Such a superposition of the strong nearest parallel and the weaker long-range antiparallel exchange interactions typically allows for the long-range spin-spiral order. Its direction ($\vec{q} \parallel [001]$) follows from the symmetry reasons: the 7-th shell, critical for setting up the AFM order, contains 8 atoms at $\vec{R} = (\pm a, 0, \pm c)$ and $(0, \pm a, \pm c)$, situated above and below the ab-plane of the central atom. The corresponding Neel temperature can be estimated from the peak of the magnetic specific heat $C_V(T)$ computed for the largest cluster size ($T_N \approx 350$ K at $R/a \approx 2.87$, see the inset in Fig. 2 b). This reasonably agrees with experimental $M(T)$ slope change, well seen at about the same temperature.

The influence of chemical disorder can be estimated by means of the CPA alloy theory [5, 6], implemented in the SPR-KKR method. By assuming 30 % of Mn(2a)/Ga(2b) disorder, as it was identified in experiment, modifies the exchange picture (Fig. 2 a). The exchange interactions within Mn(2a) sublattice, especially the nearest-neighbor ones, become slightly weaker compared to the ordered case. In addition, its statistical factor of $(1 - 0.3)^2 = 0.49$ might noticeably reduce the Neel temperature. Altogether, this coupling alone would lead to the similar magnetic order as in the fully ordered case. Similar dependency is exhibited within the extra sublattice Mn(2b), except for the 2-nd shell, which shows a noticeable antiparallel coupling to 8 atoms at $(\pm a/2, \pm a/2, \pm c/2)$, which also leads to $\vec{q} \parallel [001]$, though favoring a shorter wavelength. However, since these interactions enter with the low weight of $0.3^2 = 0.09$, they play a minor role for a final picture. The most important here is Mn(2a)-Mn(2b) coupling, which has a moderate statistical weight of $0.3 \cdot (1 - 0.3) = 0.21$, but also a huge bare amplitude of the near-neighbor interactions (note that, $J_{\mathrm{Mn}(2a)-\mathrm{Mn}(2b)}$ values shown in Fig. 2 a are downscaled by a factor of 10). In particular, within the ab-plane there is a huge antiparallel interaction of -28 meV with the 4 first-shell neighbors at $(\pm a/2, \pm a/2, 0)$, but also strong $+18$ meV parallel out-of-plane interaction with two second-shell neighbors at $(0, 0, \pm c/2)$. Alone, this combination would lead to the vertical parallel coupling of the neighboring collinear-AFM ordered ab-planes, however the last important ~ -9 meV antiparallel coupling to 8 neighbors in a 3-rd shell at $(\pm a, 0, \pm c/2)$, $(0, \pm a, \pm c/2)$ distorts this picture. Thus, to get a rough idea about the behavior of such complicated magnetic system, we simplified the corresponding Heisenberg model, by parametrizing it with effective interactions (i.e., by multiplying the bare values with corresponding statistical weights). As it follows from Fig. 2 c, the minimal cluster size which sets the AFM order remains the same, however, the T_N drops down to about 220 K (see the inset). Since this drives us away from the experimental result, it most probably indicates that the effective parametrization of the Heisenberg model is inapplicable (despite that the bare exchange interactions are correct) and the adequate description

might be achieved by treating the local effects explicitly, which requires substantially larger cluster sizes.

[1] J. R. Carvajal, *FULLPROF, a Rietveld refinement and pattern matching analysis program* (Laboratoire Leon Brillouin, CEACNRS, France, 2000).

[2] A. I. Liechtenstein, M. I. Katsnelson, V. P. Antropov, and V. A. Gubanov, J. Magn. Magn. Materials **67**, 65 (1987).

[3] H. Ebert, D. Ködderitzsch, and J. Minár, Rep. Prog. Phys. **74**, 096501 (2011).

[4] B. Bauer, L. D. Carr, H. G. Evertz, A. Feiguin, J. Freire, S. Fuchs, L. Gamper, J. Gukelberger, E. Gull, S. Guertler, et al., J. Stat. Mech.: Theory and Experiment **2011**, P05001 (2011).

[5] P. Soven, Phys. Rev. **156**, 809 (1967).

[6] D. W. Taylor, Phys. Rev. **156**, 1017 (1967).